· Article · Advances in Polar Science
doi: 10.12429/j.advps.2023.0019 June 2024 Vol. 35 No. 2: 238-251

Comparison of the precision of glacier flow rates derived from offset-tracking using Sentinel-2 and Landsat-8/9 imagery

YANG Zhibin[1,2], CHEN Zhuoqi[1,2*], LI Gang[1,2], MAO Yanting[1,2], FENG Xiaoman[1,2] & CHENG Xiao[1,2]

[1] School of Geospatial Engineering and Science, Sun Yat-sen University, and Southern Marine Science and Engineering Guangdong Laboratory (Zhuhai), Zhuhai 519082, China;
[2] Key Laboratory of Comprehensive Observation of Polar Environment (Sun Yat-sen University), Ministry of Education, Zhuhai 519082, China

Received 4 September 2023; accepted 30 December 2023; published online 30 June 2024

Abstract Offset-tracking is an essential method for deriving glacier flow rates using optical imagery. Sentinel-2 (S2) and Landsat-8/9 (L8/9) are popular optical satellites or constellations for polar studies, offering high spatial resolution with relatively short revisit time, wide swath width, and free accessibility. To evaluate and compare the precision of offset-tracking results yielded with these two kinds of data, in this study S2 and L8/9 imagery observed in Petermann Glacier in Greenland, Karakoram in High-Mountains Asia, and Amery Ice Shelf in the Antarctic are analyzed. Outliers and various systematic error sources in the offset-tracking results including orbital and strip errors were analyzed and eliminated at the pre-process stage. Precision at the off-glacier (bare rock) region was evaluated by presuming that no deformation occurred; then for both glacierized and the off-glacier regions, precision of velocity time series was evaluated based on error propagation theory. The least squares method based on connected components was used to solve flow rates time series based on multi-pair images offset-tracking. The results indicated that S2 achieved slightly higher precision than L8/9 in terms of both single-pair derived displacements and least square solved daily flow rates time series. Generally, the RMSE of daily velocity is 26% lower for S2 than L8/9. Moreover, S2 provided higher temporal resolution for monitoring glacier flow rates.

Keywords **Sentinel-2**, **Landsat**, **glacier flow rate**s, **offset-tracking**, **precision**

Citation: Yang Z B, Chen Z Q, Li G, et al. Comparison of the precision of glacier flow rates derived from offset-tracking using Sentinel-2 and Landsat-8/9 imagery. Adv Polar Sci, 2024, 35(2): 238-251, doi: 10.12429/j.advps.2023.0019

1 Introduction

Offset-tracking calculates the local offset of two images through a correlation algorithm, and then combines it with the overall offset to obtain the total displacement fields of the entire region (Li et al., 2013). This method can derive ground deformation with low correlation, fast computation, and high accuracy, allowing for monitoring glacier velocity over a long period and large area. Offset-tracking using SAR images is not highly affected by decorrelation like InSAR, because it does not rely on phase information but only employs the backscatter coefficients. Nevertheless, offset-tracking using SAR images obtained from different orbits or platforms is still difficult due to the large observation geometry differences. Although optical data is susceptible to factors such as clouds and precipitation, optical remote sensing has advantages in short

* Corresponding author, ORCID: 0000-0003-1307-4941, email: chenzhq67@mail.sysu.edu.cn

revisit period, less sensitive to surface melting, and availability of multiple data sources. The optical offset-tracking results generally include displacements in the east–west (EW) and the north–south (NS) direction, and correlation coefficients. The monitoring accuracy is generally within 1/10–1/50 pixels (Herman et al., 2011; Li et al., 2019; Peternel et al., 2017; Scherler et al., 2008). Pre-processing steps and post-processing steps to filter out noises are usually recommended to improve the precision and accuracy of displacement estimates (Zitová and Flusser, 2003).

Early scholars explored the use of single-pair optical images to monitor surface deformation and conducted a comprehensive analysis of various error sources. The "mean subtracting" method is proposed to remove the strip error (Van Puymbroeck et al., 2000). Generally, high-resolution images provide more detailed deformation fields. Delacourt et al. (2004) estimated the displacements of the LaClapière landslide using high-resolution Quickbird images, and results were consistent with the InSAR-derived results and field measurement. Berthier et al. (2005) estimated the glacier velocity in the Mont Blanc area (Alps) using SPOT5 images, which was verified with GPS observations and found accurate agreement of horizontal displacements. The emergence of Co-registration of Optically Sensed Images and Correlation (COSI-Corr) software greatly improved the monitoring accuracy and computational efficiency of optical image cross-correlation matching (Leprince et al., 2007), enabling precise registration up to 1/20 pixels. Currently, this software has been widely used in monitoring large-scale surface deformation (Leprince et al., 2008a). Debella-Gilo and Kääb (2011) investigated the impacts on image resolution to the precision of displacement estimation, and found that low spatial resolution leads to more matching errors. Debella-Gilo and Kääb (2012) proposed a method that incorporated multi-template matching and adaptive template windows into the conventional Normalized Cross Correlation (NCC) algorithm. This method reduces the error of displacement estimation and improves the SNR (Signal-to-Noise Ratio) of the matching. Offset-tracking was applied to obtain Antarctic glacier velocity by using Landsat-5 images (Bindschadler and Scambos, 1991). Since then, this method has been widely applied in studies of glaciers (Jawak et al., 2018), dunes (Ding et al., 2020), earthquakes (Ding et al., 2016), etc. He et al. (2019) used Sentinel-2 (S2) images and extracted the deformation field of the 2016 moment magnitude 7.8 Kaikoura earthquake based on COSI-Corr. A systematic analysis and correction of various types of errors is conducted for estimating the deformation fields. In addition, the comparison with deformation fields extracted from Landsat-8 (L8) images showed that S2 results had higher and finer accuracy.

Time series of displacement has higher temporal resolution derived from multi-pair images. By applying Singular Value Decomposition (SVD) inversion to obtain the deformation time series of the West Kunlun Mountains glaciers, Zheng (2015) suggested that the horizontal deformation monitoring accuracy based on L8 offset-tracking reaches 0.15 m (0.01 pixels). Li et al. (2023) proposed a weighted least squares solution based on connected components to calculate the glacier velocity time series combining the offset-tracking results yielded separately by Sentinel-1 and Sentinel-2. This method addressed the issue of zero values that may arise if applying an SVD algorithm in solving the displacement time series.

Current research tends to derive displacement or velocity time series instead of single-pair displacement to improve the temporal resolution and precision of surface deformation monitoring. With the increasing availability of optical images, it becomes more important to investigate the precision of the deformation time series derived from offset-tracking using different optical data. The Landsat series and S2 are the two widely used and freely available optical data with a large amount of achieved observations for extracting glacier flow rate (Bindschadler and Scambos, 1991; Fahnestock et al., 2016; Kääb et al., 2016; Millan et al., 2022; Mouginot et al., 2014, 2017; Paul et al., 2016; Young, 1989). Landsat series has a longer historic achieves since the 1980s, while S2 has a wider swath width and more frequent repeating cycles, but only started to accumulate observations since 2015. Given their regular acquisition plans and a large amount of observation achieves, they are widely been employed for deriving glacier velocity time series. Currently, the precision of offset-tracking is usually evaluated with the off-glacier region, but seldom evaluated with an error propagation theory based on the redundant offset-tracking on the glacierized region. Considering the texture difference, the performance of offset-tracking should be worse on glaciers since less texture is provided.

In this study, S2 and Landsat-8/9 (L8/9) images were employed to derive glacier displacement time series, and their precision was analyzed and evaluated separately. This paper introduced the data processing workflow for monitoring surface deformation by using S2 and L8/9 optical data, and analyzed the correction methods of outliers and systematic errors of the original offset-tracking results. Glacier flow rates time series of Petermann, Karakoram, and Amery in 2021 were derived from a least square method based on connected components. The error propagation theory helps to evaluate the precision of the derived velocity time series. Finally, a comparative analysis of the glacier flow velocity fields and precision derived from the two optical images was compared.

2 Study area and data

2.1 Study area

This study analyzed images obtained at three sites separately in Arctic, Antarctic and High Mountains Asia (HMA), which are Petermann Glacier, Amery Ice Shelf, and Karakoram. Petermann Glacier (80°N, 60°W) is located in

the northwest Greenland, east of the Nares Strait, and adjacent to the Arctic Ocean (Figure 1). It is one of the largest outlet glaciers in the Northern Hemisphere and one of the seven glaciers in Greenland that terminate in the ocean (Hogg et al., 2016). Petermann Glacier consists of a floating ice tongue that is ~70 km long and ~15 km wide. The thickness of the glacier varies from about 600 m at the grounding line to about 30–80 m at its front (Rignot and Steffen, 2008), with an area of ~1280 km^2 and contributes ~4% of the total ice discharge from the Greenland Ice Sheet (Rückamp et al., 2019). In the following text, "Petermann" refers to the Petermann Glacier.

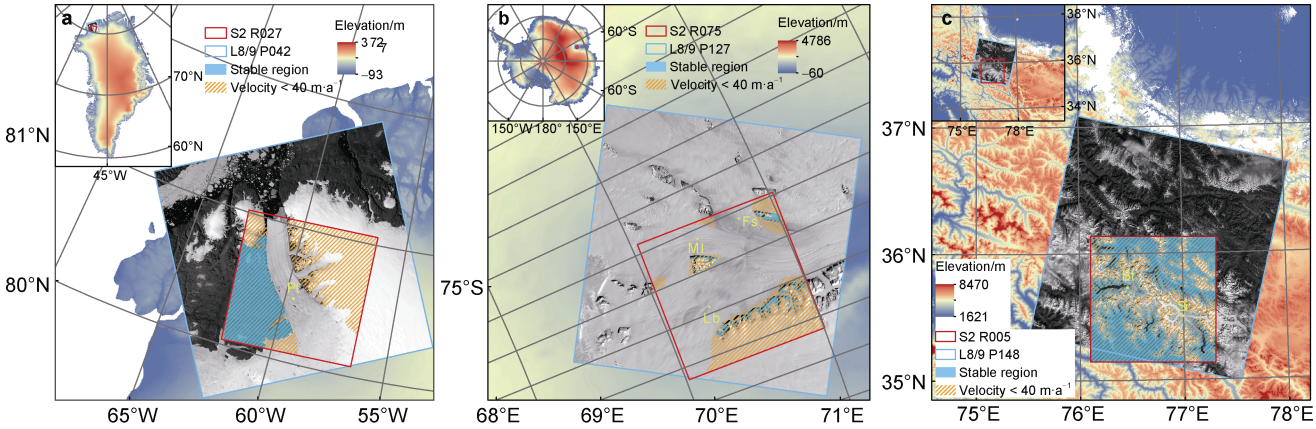

Figure 1 Study area and coverage of the optical image. **a**, Petermann; **b**, Amery; **c**, Karakoram. Background shows the topography. The yellow points mark the glaciers mentioned in context. Abbreviations: Pt = Petermann Glacier, Fs = Fisher Glacier, Ml = Mellor Glacier, Lb = Lambert Glacier, Si = Siachen Glacier, Bt = Baltoro Glacier.

Amery Ice Shelf, with an area exceeding 6000 km^2, is the largest ice shelf in East Antarctica and contributes ~16% of the ice discharge from the East Antarctic Ice Sheet (Spergel et al., 2021). The selected study area (73°S, 68°E) is located in the upstream supply region of the Amery Ice Shelf and includes the Lambert Glacier, Mellor Glacier, and Fisher Glacier (Li et al., 2020), In the following text, "Amery" refers to this area.

Karakoram is located at HMA, where is concentrated large amount of glaciers. The selected study area (36°N, 77°E) includes Siachen Glacier and Baltoro Glacier, which are two of the longest mountain glaciers in low latitude region. Locating at east Karakoram, Siachen Glacier is not only the largest glacier in the entire Karakoram range but also the largest glacier in all of HMA (Arendt et al., 2017). It has a length of ~74 km and a width ranging from 1–8 km, covering an area of ~936 km^2 (Frey et al., 2014). Baltoro Glacier, located in central Karakoram and northern Pakistan, covers an area of ~660 km^2, with a central length of ~62 km and has 12 tributary glaciers. Baltoro Glacier is extensively covered by debris, with over 38% of its area covered by glacier debris (Gibson et al., 2017; Mayer et al., 2006). In the following text, "Karakoram" refers to this region.

2.2 Data

S2 and L8/9 data are two types of free accessible optical data with relatively high spatial resolution, high revisit frequency, and wide swath width, making them suitable for long-term glacier velocity monitoring. L8/9 refers to the eighth and ninth satellites in the Landsat program series, which were launched in February 2013 and September 2021, respectively. They carry the Operational Land Imager (OLI) and OLI-2 sensors, respectively, with 9 bands, a spatial resolution of 30 m (15 m for the panchromatic band), and a swath width of 185 km. S2 is a group of satellites in the European Space Agency's (ESA) Sentinel series, including Sentinel-2A and -2B, which were launched in June 2015 and March 2017, respectively. The spatial resolution of S2 ranges from 10 m to 60 m, with 13 bands. Furthermore, the imagery data from L8/9 and S2 have been orthorectified using external DEM (Ali et al., 2020; Ding et al., 2020), reducing the difficulty in offset-tracking. They can be directly applied to COSI-Corr for deriving deformation fields. In this study, the panchromatic (Pan) band of L8/9 and the NIR band from S2 were selected for offset-tracking. Parameters of selected data are shown in Table 1.

Table 1 The parameters of the S2 and L8/9

Optical sensor	S2-A/B	L8/9
Imaging band	NIR, Band 8	Pan, Band 8
Resolution/m	10	15
Revisit time/d	10 (1 sat) 5 (2 sat)	16 (1sat) 8 (2 sat)
Product level	Level-1C	Level-1T
Track	Orbit: 27/75/5 Tile: 21XVK/42CVD/43SFV	Path: 42/127/148 Row: 1/112/35

This study adopted 72 scenes of S2 images obtained from the ESA (https://scihub.copernicus.eu/dhus/#/home) and 56 scenes of L8/9 images obtained from the U.S. Geological Survey (USGS) (https://earthexplorer.usgs.gov) (Table 2). These images are cloud-free or with slight cloud coverage. Only S2-B imagery was available for Amery, while S2-A acquisitions were not available.

Table 2 Detailed information of the selected optical images

Area	Sensor	Track	Image counts	Acquisition dates	Average intervals/d
Petermann	S2	R027	25	2022-03-14–2022-09-15	7.71
	L8/9	P042	19	2022-03-26–2022-09-26	9.68
Amery	S2	R075	14	2021-09-19–2022-03-08	12.14
	L8/9	P127	15	2021-09-19–2022-03-30	12.8
Karakoram	S2	R005	33	2022-01-12–2022-11-28	9.7
	L8/9	P148	22	2022-01-12–2022-12-22	15.64

At Petermann, the Greenland Ice Sheet Mapping Project (GIMP) DEM product (NSIDC-0645), single-pair velocity maps from optical images (NSIDC-0777) and annual velocity product (NSIDC-0725) provided by the National Snow and Ice Data Center (NSIDC) in the United States were applied for base maps plotting, selecting the low-velocity region, and comparison of single-pair velocity precision. Their resolutions were 90, 100 and 200 m, respectively.

At Amery, the 1 km resolution Antarctic DEM product (NSIDC-0422) was applied, which combines measurements from the European Remote Sensing Satellite-1 (ERS-1) and the Ice, Cloud, and land Elevation Satellite (ICESat). The stable region is set to the Antarctic Exposed Rock product (https://data.bas.ac.uk/items/cbacce42-2fdc-4f06-bdc2-73b6c66aa641/). Antarctica ice velocity product (NSIDC-0754) served as reference velocity fields, which combined interferometric phase from multiple satellite synthetic aperture radar systems. Since no current data are available, this study used the 2018 annual velocity fields of Antarctica with 450 m resolution.

At Karakoram, the 30 m resolution SRTM1 (Shuttle Radar Topography Mission) DEM from USGS was applied. The extraction of the stable region was conducted with the Randolph Glacier Inventory (RGI) 6.0 product (NSIDC-0770). HMA annual velocity product (NSIDC-0776) from the Inter-Mission Time Series of Land Ice Velocity and Elevation (ITS_LIVE) project (Gardner et al., 2019) was used, with 240 m resolution.

3 Methods

COSI-Corr plugin of ENVI software was employed to generate original offset-tracking outputs with displacements in the EW and NS directions. Then the gross and systematic errors of the offset-tracking results were evaluated and removed. The least squares solution based on connected components was then used to calculate the displacement time series for these two platforms, and the precision of the flow rates time series from both platforms was analyzed and evaluated (Li et al., 2023). The experimental workflow shows in Figure 2.

3.1 Image pairs selection

Including too many image pairs will increase the computing time cost without significant accuracy improvement, this study only performed offset-tracking of each acquisition with its closest next three acquisitions.

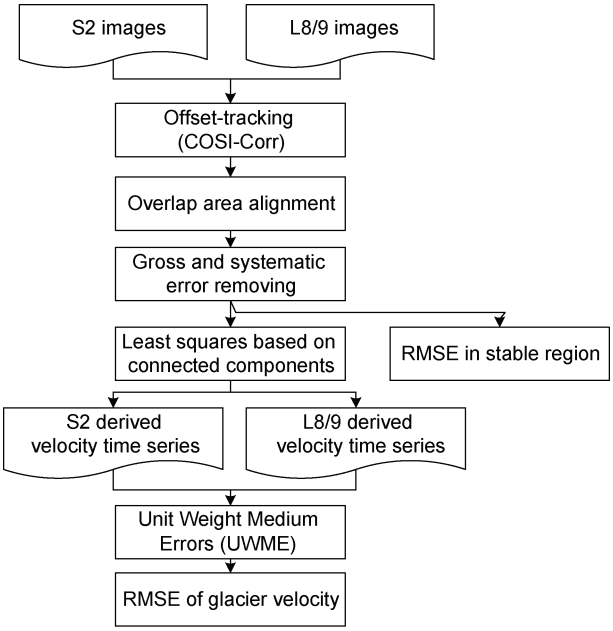

Figure 2 Working flow of this research.

3.2 Offset-tracking

COSI-Corr is an ENVI plugin based on IDL, which is mainly used for precise orthorectification, image registration, correlation of optical images, and offset-tracking (Ayoub et al., 2015; Leprince et al., 2007). Frequency domain image correlation was used to obtain the EW and NS deformations in this study. The monitoring precision was reported as 1/20 pixels (Konca et al., 2010). Key parameters are listed in Table 3. The step determines the spatial resolution of the offset-tracking results, that is larger step size resulting in lower spatial resolution of the outputs, and vice versa. Considering the size of the experimental area and the image resolution of S2 and L8/9, the displacement steps were set to 9 and 6, respectively, to achieve a unified spatial resolution of 90 m for the output displacement fields. Due to the inconsistent coverage of S2 and L8/9 images, the L8/9 offset-tracking results were cropped based on the range of S2 images for convenient comparative analysis of the two types of data.

Table 3 The parameters of COSI-Corr

	S2	L8/9
Initial window	128	128
Final window	32	32
Step	9	6
Robustness	5	5
Mask threshold	0.9	0.9

3.3 Gross and systematic errors analysis and removing

Optical image matchings are susceptible to orbit error, strip error and noise (Ding et al., 2016; He et al., 2019). The first two are systematic errors and should be evaluated and removed, while noise is the random error. The results of removing systematic errors are here presented by using S2 as an example. Figure 3 shows the offset-tracking field for 13–18 April 2022 of Petermann and its surrounding area. Different types of error sources can be identified, including decorrelation noise, orbit error, and strip error. The first is the gross error, while the last two are systematic errors. Decorrelation noise is mainly caused by the variation in the surface radiometric properties, resulting in abnormal deformation values. Orbit error is mainly caused by systematic offsets in optical images at different times, resulting in a gradual overall shift. Strip error is mainly caused by misalignment of charge-coupled devices (CCDs) in push-broom sensors, resulting in periodic parallel band-like signals in the offset-tracking results along the satellite's flight direction. Since the precision analysis was designed for evaluating random error, these gross and/or systematic error sources should be evaluated and removed properly. For S2, the offset-tracking results were also found with satellite attitude angle error, which was distributed along the satellite's flight direction. This error was affected by terrain undulation and vegetation cover et al (Van Puymbroeck et al., 2000) and affected little to extract flow rates in the polar region and the removal step was not required here. Methods of removing these three kinds of errors are as follows.

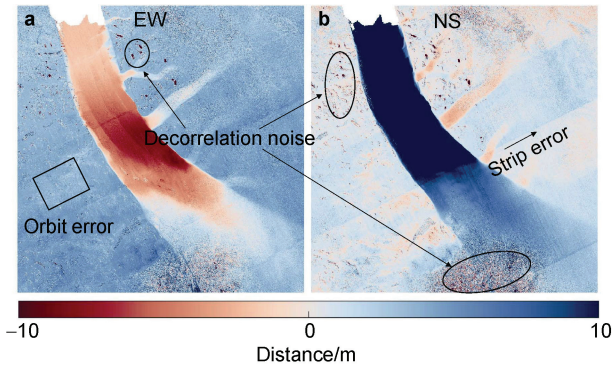

Figure 3 Gross and systematic error sources of S2 image pair (2022-04-13–2022-04-18). **a**, EW direction deformation; **b**, NS direction deformation.

3.3.1 Decorrelation noise

Low SNR indicates less reliability of the offset-tracking results, mainly due to temporal decorrelation, terrain shadow factors, and cloud (Konca et al., 2010; Michel and Avouac, 2006). To remove the decorrelation noise, an SNR threshold (0.9 in this study) was set to mask the low threshold areas (Song, 2021). However, the SNR threshold alone cannot effectively remove all decorrelation noise. It is also necessary to remove outliers based on the spatial similarity of glacier velocity fields. In this study, the "rmoutliers" function in MATLAB with the "median" method was mainly used for outlier removal.

3.3.2 Orbit error

The S2 Level-1C data only undergoes a rough orthorectification, and there are still geometric systematic offsets in optical image pairs, resulting in a gradual overall shift in the offset-tracking results, called the orbit error (He et al., 2019). This study selected reference region for evaluating the orbit error, including low-velocity and off-glacier (bare rock) regions, and then subtracted the evaluating orbit error from the original deformation field. The off-glacier region is presumed as no deformation, while the real deformation is unknown in the glacier region. However, the off-glacier region is not uniformly distributed or not large enough for estimating, especially for Amery. The low-velocity region (Figure 1, velocity < 40 $m \cdot a^{-1}$) was calculated regarding the annual velocity products (NSIDC-0725/0754/0776), and then, off-glacier and low-velocity region are both regarded as the reference region. It can be presumed seasonal fluctuation at low-velocity regions is close to zero. A bilinear polynomial model was employed to evaluate orbit error (Lin et al., 2017):

$$R_{\text{orbit}}=a_0+a_1x+a_2y+a_3xy, \quad (1)$$

where x, y are the coordinates of the original offset-tracking results, a_0, a_1, a_2, a_3 are the coefficients of the bilinear polynomial model. After calculating the presumed velocity fields at the low-velocity region and off-glacier region according to annual velocity products, subtracting presumed deformation in the reference region from the single-pair offset-tracking result, leaving only orbit error. Then, the least square method was applied to solve 4 coefficients of the bilinear model. The model was then applied to the entire offset-tracking fields to remove the orbit error. Figure 4 compares the offset-tracking results before and after the orbit error removal, taking offset- tracking of S2 images observed on 13–18 April, 2022 as an example.

Figures 4b and 4e represent the modeled EW and NS orbit errors, respectively. After removing the orbit error, there is a noticeable improvement in the offset-tracking results (Figures 4c and 4f).

3.3.3 Strip error

Most push-broom imaging satellites, such as S2, Landsat series, and SPOT series, suffer from CCD misalignment

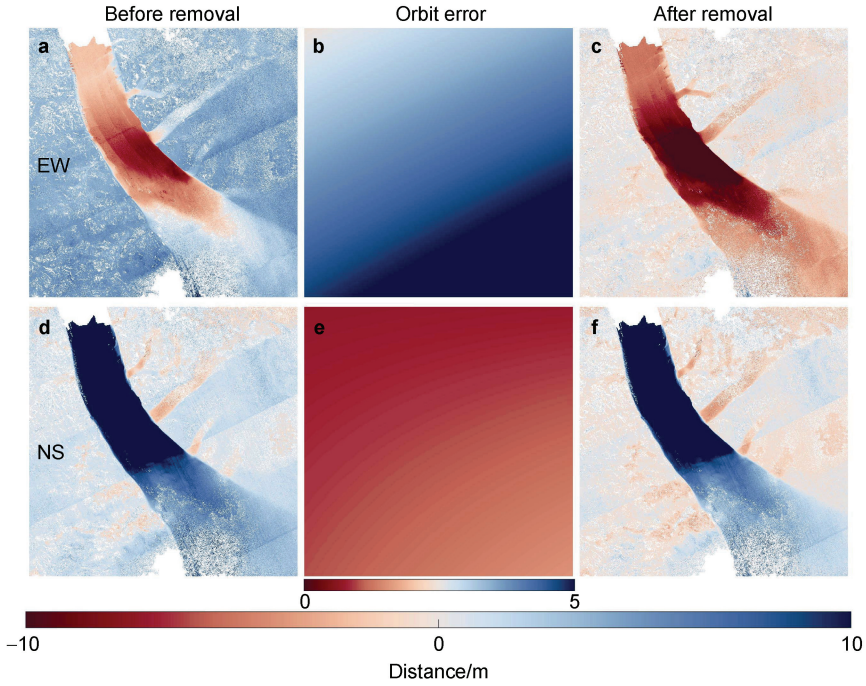

Figure 4 Comparison the offset-tracking results before and after removal of the orbit error. **a** and **d**, deformation in EW and NS direction; **b** and **e**, the simulated orbit error; **c** and **f**, deformation after removal of orbit error.

issues, which are challenging to correct (Leprince et al., 2008b; Michel and Avouac, 2006). The displacement obtained from such optical images exhibits periodic parallel striping signals along the satellite's flight direction. S2 adopts 12 staggered detectors to cover the field of view (Drusch et al., 2012). Figure 5 shows the detector footprints of S2 at Petermann.

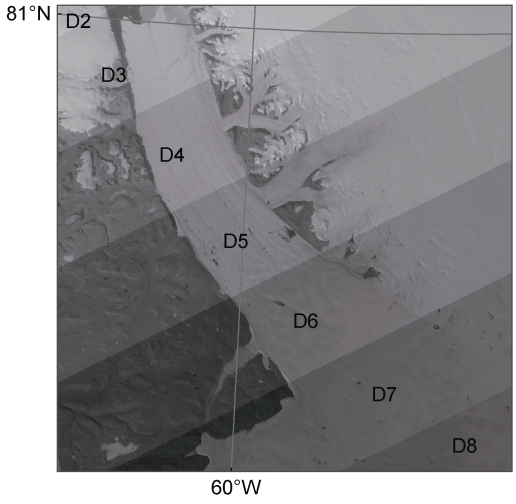

Figure 5 Detector footprints of S2 tile for relative orbit R027. D2–D8 represent different detectors.

Figure 6 shows the example of S2 images offset-tracking result of 13–18 April, 2022 to compare before and after the removal of strip error. There are noticeable strip errors which exhibit a regular distribution along the satellite flight direction in the deformation field (Figures 6a and 6d). Such errors are commonly removed using the "mean subtraction method" as follows (Ding et al., 2016; Van Puymbroeck et al., 2000).

(1) For an original offset-tracking result, select a set of pixels where are stable or deformations are known or can be presumed, and then subtract the presumed deformation from these pixels, leaving only the strip error. Here, the annual velocity product was used as a reference for calculating the presumed deformation in low-velocity areas.

(2) Align the strip error approximately along the vertical direction by rotating the deformation map of the low-velocity area counterclockwise by an angle α (α is the angle between the line mn (Figure 6d) and the column direction. In this example, $\alpha \approx 64°$).

(3) Calculate the average value of all pixels in each column of the rotated deformation map. If there was no strip error, the average value should be zero. The more significant the strip error signal, the larger the absolute value of the average.

(4) Subtract the average deformation value of each column from the deformation values of individual pixels in the original deformation map.

(5) Rotate the deformation map. After subtracting the average values, rotate by the angle α clockwise to obtain the deformation map with the strip error removed.

Noticeable strip errors are found in both the EW and NS directions (Figure 6). The mean subtraction method has effectively removed the strip error. Although theoretically there might be strip error in the results of the L8/9 as well, it found the offset-tracking results did not exhibit significant

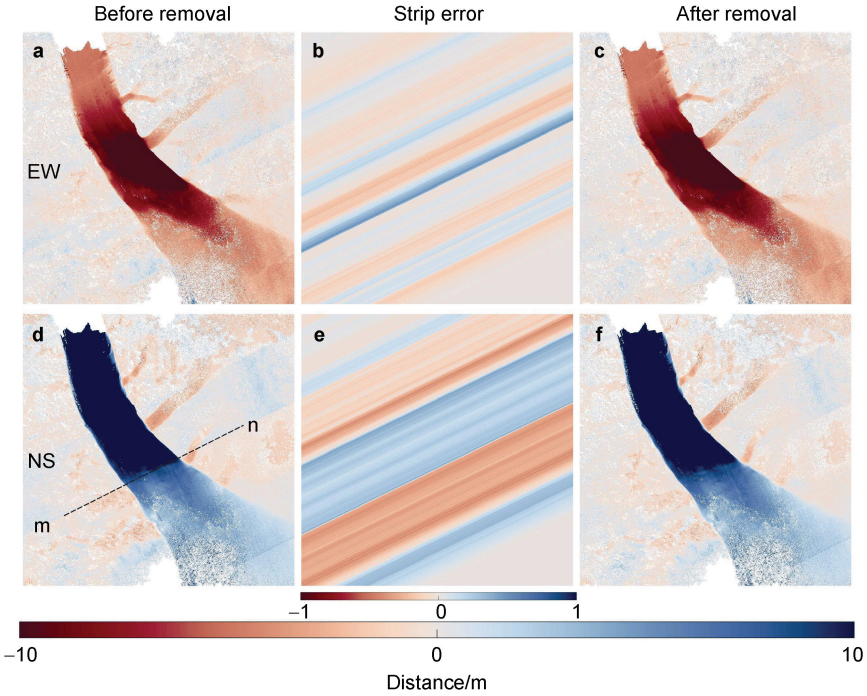

Figure 6 Comparison before and after removal of strip error. **a** and **d**, deformation in EW and NS direction; **b** and **e**, the simulated strip error; **c** and **f**, deformation after removal of strip error.

strip error. Therefore, the L8/9 was not processed to remove strip errors.

Table 4 shows the effects of removing orbit error and strip error. The mean value is the average at the reference region including low flow rates part on glaciers and bare rock part. Standard deviation (STD) roughly describes the random error of offset-tracking. For the 10 m resolution S2 images, the precision is about 1/10 pixel (1 m). Besides, the results clearly show that removing systematic error improves the precision.

Table 4 Precision of S2 images offset-tracking (2022-04-13–2022-04-18) at Petermann

	Stage of error removal	EW	NS
Mean/m	Before orbit error removal	4.059	0.943
	After orbit error removal	0	0
	After strip error removal	−0.003	0.010
STD/m	Before orbit error removal	1.146	0.991
	After orbit error removal	0.953	0.981
	After strip error removal	0.931	0.921

3.4 Flow rates time series

A least squares method based on connected components for solving velocity time series was employed, and the error propagation theory was applied to perform precision analysis (Li et al., 2023). Each acquisition date is considered as a vertex (node), and the valid offset-tracking results serve as edges. For any pixel, after removing outliers, all temporal connected components with more than two vertices are identified and processed with a least square method. If each acquisition is offset-tracked with its three subsequent dates without any outliers (gross errors), only one connected component is generated for any pixel. However, after removing outliers, there are usually multiple connected components, and each component is solved separately using the least squares method. Within a connected component, each valid offset-tracking result forms an error equation, with the offsets between adjacent dates being the unknowns. The matrix equation is represented as:

$$\boldsymbol{BX}=\boldsymbol{D}, \tag{2}$$

where $\boldsymbol{D}$ is the observations (offset-tracking results), $\boldsymbol{X}$ is the unknowns; and $\boldsymbol{B}$ is an $m\times(n-1)$ coefficient matrix (m edges and n vertices) that describes how those offset-tracking results are connected between these vertices. If no outliers were removed, the matrix $\boldsymbol{B}$ should be:

$$\boldsymbol{B}=\begin{bmatrix} 1 & 0 & 0 & 0 & \cdots & 0 \\ 1 & 1 & 0 & 0 & \cdots & 0 \\ 1 & 1 & 1 & 0 & \cdots & 0 \\ 0 & 1 & 0 & 0 & \cdots & 0 \\ 0 & 1 & 1 & 0 & \cdots & 0 \\ 0 & 1 & 1 & 1 & \cdots & 0 \\ \vdots & \vdots & \vdots & \vdots & & \vdots \\ 0 & 0 & 0 & 0 & \cdots & 1 \end{bmatrix} \tag{3}$$

The optimal estimate $\hat{\boldsymbol{X}}$ obtained through the least square method is:

$$\hat{\boldsymbol{X}}=(\boldsymbol{B}^{\mathrm{T}}\boldsymbol{P}\boldsymbol{B})^{-1}\boldsymbol{B}^{\mathrm{T}}\boldsymbol{P}\boldsymbol{D} \tag{4}$$

where $\boldsymbol{P}$ is the weight matrix. For each offset-tracking result $\boldsymbol{D}_1,\cdots,\boldsymbol{D}_m$, the weights are set as $\boldsymbol{P}_1,\cdots,\boldsymbol{P}_m$, respectively. Since the time series offset-tracking is based on optical image tracking results from the same platform and the time baseline is short, $\boldsymbol{P}$ is set as the identity matrix $\boldsymbol{E}$, that is all individual offset-tracking observations are equally weighted. The residual of the observations is:

$$\boldsymbol{V} = \boldsymbol{B}\hat{\boldsymbol{X}} - \boldsymbol{D}, \tag{5}$$

Let

$$\boldsymbol{N}_{\boldsymbol{BB}} = \boldsymbol{B}^{\mathrm{T}}\boldsymbol{P}\boldsymbol{B}, \tag{6}$$

and $\boldsymbol{Q}_{\hat{\boldsymbol{X}}\hat{\boldsymbol{X}}}$ is:

$$\boldsymbol{Q}_{\hat{\boldsymbol{X}}\hat{\boldsymbol{X}}} = \boldsymbol{N}_{\boldsymbol{BB}}{}^{-1} = (\boldsymbol{B}^{\mathrm{T}}\boldsymbol{P}\boldsymbol{B})^{-1}, \tag{7}$$

where $\boldsymbol{B}$ and $\boldsymbol{N}_{\boldsymbol{BB}}$ solely depend on the connectivity between these vertices (acquisitions).

3.5 Precision analysis

The residual can be used to quantitatively assess the precision of the velocity time series derived from S2 and L8/9 images offset-tracking, respectively. According to the error propagation law, the unit weight medium errors (UWME, $\hat{\sigma}_0$) of each connected component can be evaluated:

$$\hat{\sigma}_0 = \sqrt{\frac{\boldsymbol{V}^{\mathrm{T}}\boldsymbol{P}\boldsymbol{V}}{m-(n-1)}}, \tag{8}$$

where m is the number of valid offset-tracking results (edges) and n is the number of independent dates (vertices). Since the $\boldsymbol{P}$ matrix is an identity matrix, $\hat{\sigma}_0$ represents the RMSE of single-pair offset-tracking observations. Then the RMSE $\sigma_{\hat{x}_i\hat{x}_i}$ of the ith evaluated unknown x_i is calculated:

$$\sigma_{\hat{x}_i\hat{x}_i} = \hat{\sigma}_0\sqrt{\boldsymbol{Q}_{\hat{x}_i\hat{x}_i}}, \tag{9}$$

where $\sigma_{\hat{x}_i\hat{x}_i}$ is the ith element in the diagonal of the cofactor matrix $\boldsymbol{Q}_{\hat{x}\hat{x}}$. $\sigma_{\hat{x}_i\hat{x}_i}$ is the RMSE of the displacement between the two dates solved, and then RMSE of the daily velocity is calculated by dividing the temporal intervals between each adjacent acquisition.

In assessing the precision, two methods are employed for off-glacier (bare rock) zone and glacier zone separately. For off-glacier region, where no deformation is expected, the RMSE (E_{RMSE}) is used for precision assessment with formula (10).

$$E_{\mathrm{RMSE}} = \sqrt{\frac{1}{m}\sum_{i=1}^{m} y_i^2}, \tag{10}$$

where m is the total number of pixels in the off-glacier area, y_i is the evaluated displacement.

Moreover, for both bare rock regions and glacier areas with deformation and a lack of ground truth data, the UWME and the RMSEs of displacement and velocity were evaluated based on error propagation analysis. The reason for separate calculations is that the surface textures differ significantly between off-glacier and glacier areas, and different textures can affect the precision of offset-tracking. Additionally, cross-validation was used when using two different kinds of data sources. And 37 pairs of offset results from S2 and L8/9 images at similar times were selected for comparative analysis in cross-validation.

4 Results

4.1 RMSE at off-glacier region

After removing various gross and systematic errors, the RMSE of the displacements in the off-glacier region for single-pair offset-tracking results are calculated (Figure 7). The EW and NS directions are represented by the x-axis and y-axis, respectively. It can be observed that the RMSE of S2 ranges from 0.4–1.2 m, while the RMSE of L8/9 ranges from 0.8–1.2 m. This indicates that the single-pair displacements of S2 show slightly higher precision. However, S2 shows a wider distribution of RMSEs than L8/9, which is possibly due to the proposed method of removal of strip error in case of offset-tracking to S2-A–S2-B is not as good as that to L8/9. However, in the case of the offset-tracking to images observed with the same satellite (S2-A–S2-A, and/or S2-B–S2-B), the RMSE was lower than L8/9, due to its higher resolution and shorter acquisition intervals.

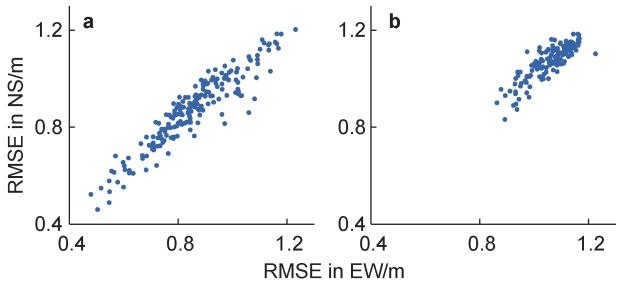

Figure 7 RMSEs for single-pair displacements of S2 (**a**) and L8/9 (**b**). The x-y axis represents RMSE in EW and NS direction.

4.2 Glacier flow rates

For offset-tracking in three study areas, 198 image pairs from 72 S2 images and 144 image pairs from 56 L8/9 images were selected and formed daily velocity time series. Figure 8 shows the average flow rate fields in both EW and NS directions that derived from different platforms for the three study sites. The flow rates calculated by both platforms are very close in both directions and magnitude. The dates were different for three sites due to polar night, it obtained summer velocity at Petermann and Amery, while annual velocity for Karakoram. Petermann's daily velocity in summer was highest, up to 4 m·d^{-1}; followed by Amery's up to 3 m·d^{-1}. The study area was not the ice front at Amery Ice Shelf, which might account for lower rates than at Petermann. The lowest velocity in Karakoram was up to

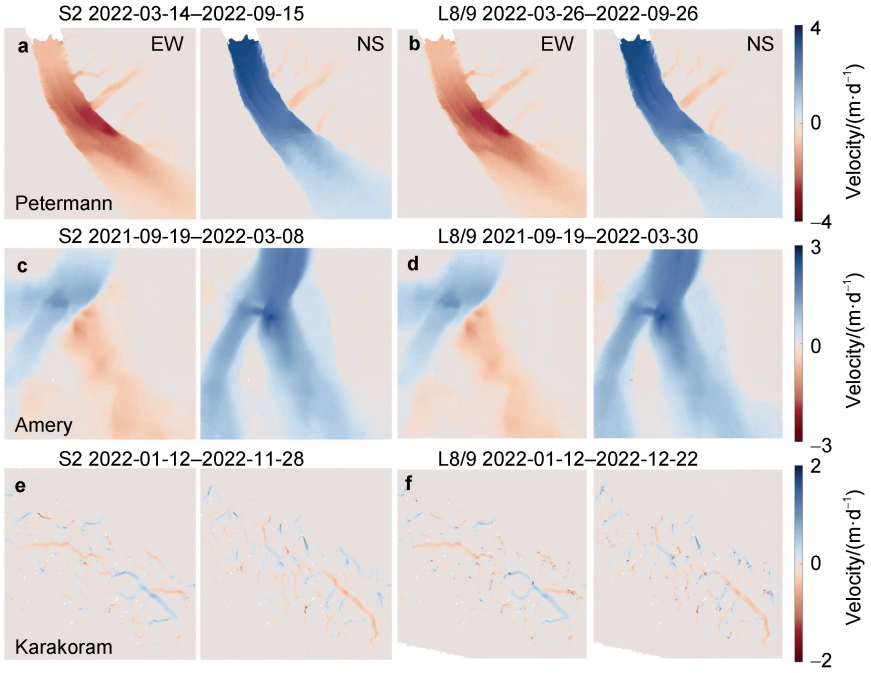

Figure 8 Average flow rate maps derived from S2 (**a**, **c**, **e**) and L8/9 (**b**, **d**, **f**). The first row shows Petermann, the second row shows Amery, the third row shows Karakoram; Columns 1 and 3 show rates in EW direction, columns 2 and 4 show rates in NS direction.

2 m·d^{-1} for the annual average. The flow rates derived from S2 are smoother than with L8/9, indicating less noise, especially at the upper zones of glaciers. The average acquisition intervals for S2 at Petermann, Amery, and Karakoram are 7.71, 12.14, and 9.7 d, respectively; while for L8/9, they are 9.68, 12.8, and 15.64 d, respectively. Therefore, S2 provides higher temporal resolution for calculating flow rates time series compared to L8/9.

Due to the influence of incoherent noise, there are lots of gaps (no valid offset-tracking outputs) in the original offset-tracking results. The redundant offset-tracking and least squares method based on connected components addressed this issue to some extent. However, there are still gaps (no data) in the flow rates time series, and the valid data coverage of the flow rates time series is presented in Figure 9, a higher value indicates fewer gaps. The valid data coverage of S2 is generally higher than L8/9, indicating that S2 derived results show fewer gaps. The valid coverage of both S2 and L8/9 results is mostly above 0.8. Results with below 0.8 mainly occur in the summer, due to the high temperatures induced surface melting, leading to less valid offset-tracking results.

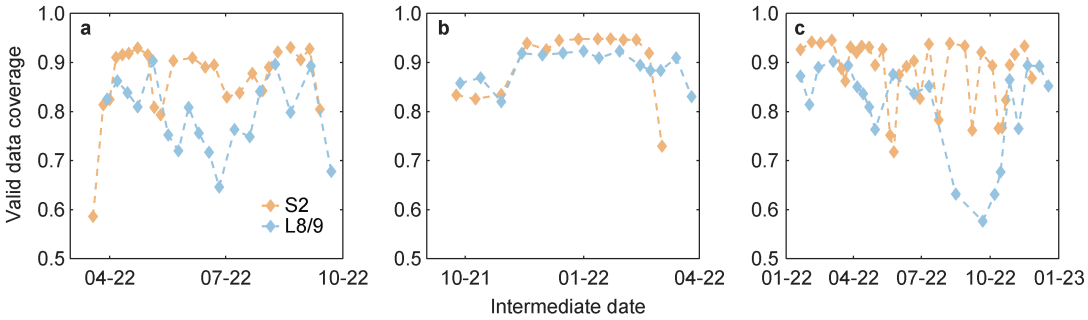

Figure 9 Valid coverage of derived glacier flow rate maps. **a**, Petermann; **b**, Amery; **c**, Karakoram. The *x*-axis is the middle date between the start and end dates of an image pair; the *y*-axis is valid data coverage of flow rates time series.

4.3 Offset-tracking precision

The histogram of the UWME (representing the precision of single-pair offset-tracking) in glacier and off-glacier regions are exhibited in Figure 10. Amongst the three experimental regions, the UWME in the glacier and off-glacier regions exhibit similar trends. The UWME in off-glacier region is notably lower, signifying a higher precision. The peak value of S2 is higher than L8/9, and its range is lower than that of L8/9, indicating that S2 exhibits significantly higher precision than L8/9. At Amery, the interval corresponding to the peak value in the histogram is the smallest, indicating the best precision in that area. However, the histogram is right-skewed, indicating the

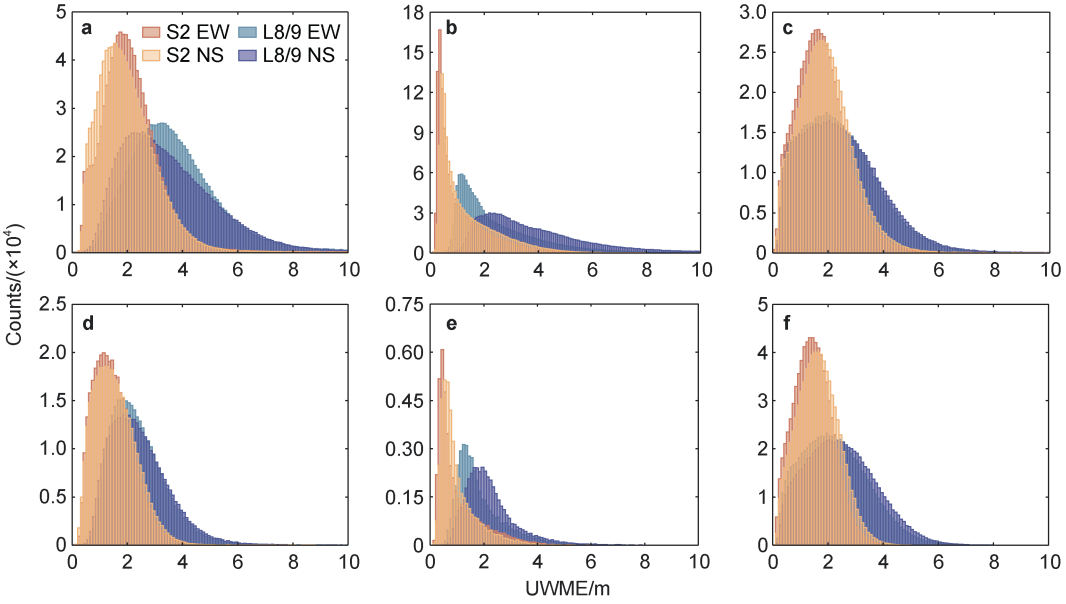

Figure 10 Histogram of UWME distribution in glacier (**a**, **b**, **c**) and off-glacier (**d**, **e**, **f**) regions. **a** and **d**, Petermann; **b** and **e**, Amery; **c** and **f**, Karakoram. The *x*-axis represents UWME; the *y*-axis is the counts of pixels.

gross errors were possibly not fully removed. Additionally, the UWME in glacier region of S2 is mainly within 4 m, while that of L8/9 is mainly within 6 m; and the UWME in the off-glacier region of S2 is mainly within 3 m, while that of L8/9 is mainly within 4 m. For the glacier region, the peak columns RMSE histograms for S2 derived results are 1.65, 0.40 and 1.70 m for Petermann, Amery and Karakoram, respectively (average of EW and NS); while for L8/9 derived results, they are 2.85, 1.66 and 1.95 m.

Figure 11 shows the error propagation evaluated RMSEs of daily velocity in the glacierized and off-glacier region, by presuming the ideal situation which no outliers are removed. The *y*-axis represents the RMSEs of daily velocity, while the *x*-axis represents the middle date between the start and end dates of each image pair. At Petermann and Amery, the precision of S2 is significantly higher than that of L8/9, as indicated by the curve of S2 mostly lying above that of L8/9. At Karakoram, the precision of S2 and L8/9 is comparable, with both within 0.25 m and showing variations. The RMSEs in the glacier and off-glacier areas fluctuate consistently, while the RMSEs are lower in the off-glacier region. Furthermore, RMSEs of the same platform at the off-glacier area exhibit minimal discrepancies in EW and NS directions, suggesting a substantial overlap between the two curves. Overall, S2 exhibits better precision compared to L8/9. Combining these results with the RMSE and UWME above, it can be concluded that both platforms exhibit good precision in estimating the flow rates time series, but S2 performs slightly better than L8/9. Specifically, for the glacierized region, the average ideal RMSE at the glacier region for S2 derived results are 0.210, 0.064 and 0.154 m·d^{-1} for Petermann, Amery and Karakoram, respectively (average of EW and NS); while for L8/9 derived results, they are 0.286, 0.164 and 0.129 m·d^{-1}. RMSE for S2 is ~26% lower than L8/9. Much longer intervals (Table 2) of L8/9 result in its higher precision of daily velocity than S2.

S2 solves a lower UWME because it represents the RMSE of single-pair offset-tracking observations. Considering the same precision of offset-tracking in terms of pixel level, S2 should yield higher precision in terms of meters. Although the acquisition intervals are smaller for S2 than L8/9, the former still solves a smaller RMSEs of the daily velocity, except for Karakoram, possibly due to large difference of acquisition interval differences.

The cross-validation to S2 and L8/9 derived velocity taken at the similar time (Figure 12). The R^2 is 0.9678 and RMSE is 0.2226 m·d^{-1}, indicating good consistency and a small difference in the offset-tracking results between the two platforms.

Finally, we compared the single-pair offset-tracking derived velocity in this study with the published single-pair velocity products from optical images (L8 and S2) at Petermann. No single-pair velocity products were found for the same period at Karakoram and Amery. We selected 22 image pairs of S2 and 12 image pairs of L8, then calculated the STD of velocity at off-glacier region (Figure 13a) and mean velocity at glacier region (Figure 13b). Average STD in off-glacier regions for NSIDC-0777 were 0.52 m·d^{-1} and 0.28 m·d^{-1} for L8/9 and S2, respectively; and for the results of this study were 0.37 m·d^{-1} and 0.21 m·d^{-1} for L8/9 and S2, respectively (Figure 13a). In terms of average glacier velocity (Figure 13b), STD of the average velocity differences between NSIDC-0777 and this study derived results were 0.18 m·d^{-1} and 0.29 m·d^{-1}. Similar fluctuation trends can be seen in Figure 13b.

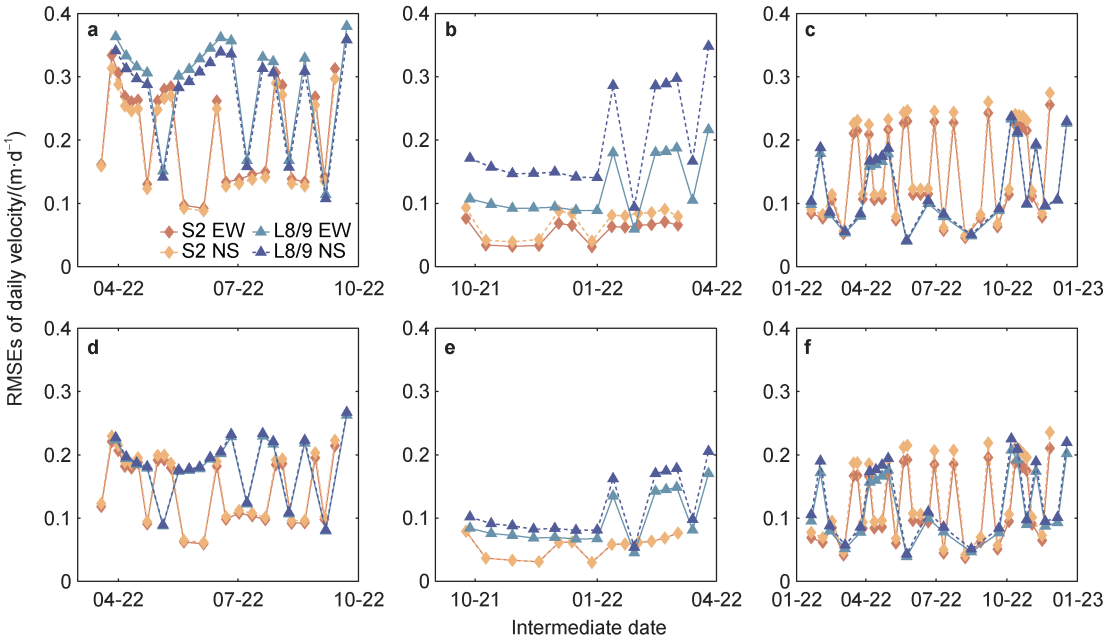

Figure 11 Ideal RMSEs of daily velocity time series in glacier (**a**, **b**, **c**) and off-glacier (**d**, **e**, **f**) region. **a** and **d**, Petermann; **b** and **e**, Amery; **c** and **f**, Karakoram. The *x*-axis is the middle date between the start and end dates of an image pair; the *y*-axis is RMSEs of daily velocity.

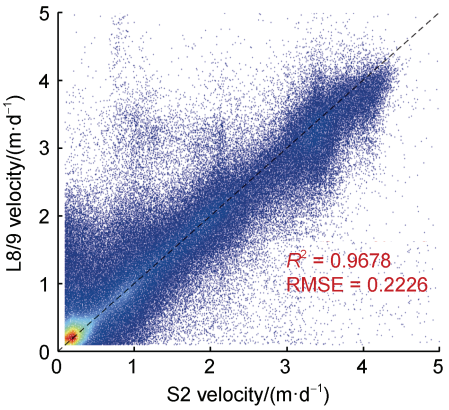

Figure 12 Cross-validation of S2 and L8/9 evaluated glacier daily flow rates. The *x*-*y* axes represent daily velocity of S2 and L8/9.

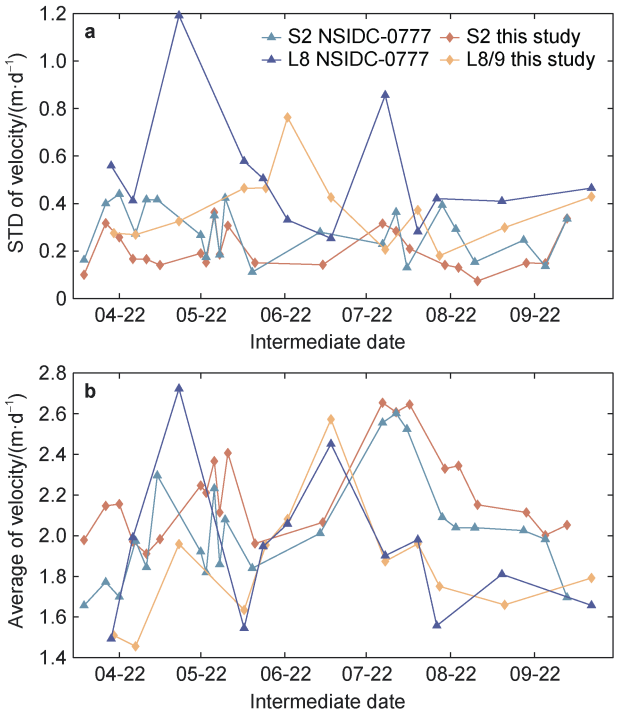

Figure 13 Comparison of single-pair velocity between this study and NSIDC-0777 velocity product. **a**, the standard deviation at off-glacier region; **b**, the average velocity of Petermann.

5 Discussion

5.1 Factors affecting the precision of offset-tracking

Monitoring surface deformation requires good-quality optical imagery. The estimation of optical image displacement is susceptible to factors such as satellite flight attitude disturbances and CCD misalignment. Additionally, it can be affected by disturbances such as terrain undulations, cloud cover, and precipitation. These factors introduce various types of systematic errors into the deformation field, including decorrelation noise, orbit errors, strip errors, and terrain shadow errors (Ding et al., 2016; He et al., 2019).

In this study, the RMSE of the stable region in the experimental area was used to quantify the effects of error removal (decorrelation noise, orbit errors, and strip error) at each stage of error processing for different platforms (Figure 14). After removing the decorrelation noise, the

RMSE for single-pair displacements from the S2 and L8/9 are within ~5 m, indicating that the orbit errors cause the largest abnormal deformation values. After removing the orbit errors, the RMSEs of both S2 and L8/9 significantly decrease, and both are within ~1.2 m. Removing the strip error also reduces the RMSE of S2 (Table 4). The red dots (after removing the strip error) are lower than the blue dots (before removing the strip error) by ~0.001 m (Figures 14a, 14c), indicating a reduction in the error of CCD misalignment.

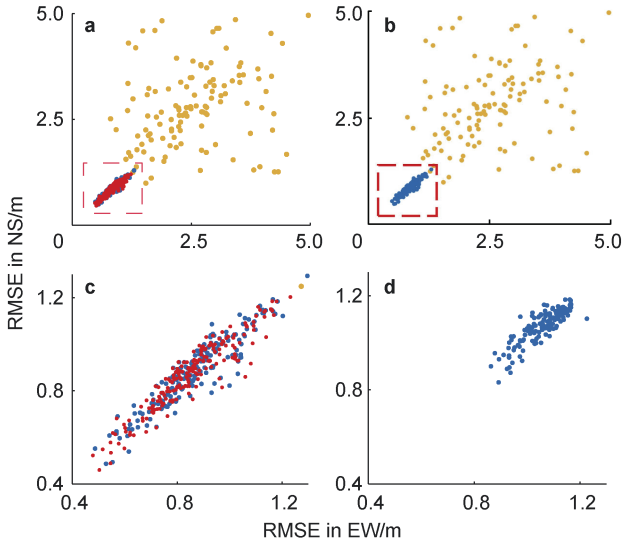

Figure 14 RMSE before and after error removal. **a**, S2; **b**, L8/9; **c**, S2 from red box in (**a**); **d**, L8/9 from red box in (**b**). The *x*-*y* axes represent the RMSE in EW and NS direction, respectively. The yellow, blue and red points mark the RMSE after removal of decorrelation noise, orbit error, and strip error, separately.

Removing the systematic errors is a necessary and common process for extracting flow rate, although the error cannot be completely removed. Assessing and removing the strip error of can be difficult if the reference regions are not large enough or well distributed. For example, in the D8 area of Figure 5.

5.2 Theoretical and actual precision of offset-tracking

In this study, the COSI-Corr was used for offset-tracking. Although the theoretical precision of COSI-Corr reaches 1/20–1/50 pixels (Leprince et al., 2007); in the actual cross-correlation calculations, it is susceptible to various errors, and the actual precision is expected to be lower. Assuming a theoretical precision of 1/20 pixels, the theoretical precision of deformation monitoring for S2 and L8/9 should be 0.5 m and 0.75 m in any direction, respectively. He et al. (2019) obtained an RMSE of 0.6–1.1 m for coseismic deformation results using S2 data. Song (2021) obtained an RMSE of ~0.51 m and 0.78 m for landslide deformation results using S2 and L8 data, respectively. In this study, after removing systematic errors, the RMSE in the stable region for single-pair displacements from S2 is generally in the range of 0.4–1.2 m, and for L8/9, it is generally in the range of 0.8–1.2 m (Figure 14). The precision on ice is obviously lower than the theoretical precision, possibly due to smoother texture in the polar region than most of the world. Still, the precision of S2 is higher than L8/9 and generally consistent with the theoretical precision.

5.3 Limitations

For comparing the precision of flow rates time series offset-tracking for different optical platforms, several limitations were identified in this study.

(1) In consideration of factors such as spatial resolution, revisiting time, imaging swath width, amount of the achieved data, and acquisition cost, this study employed medium to high-resolution optical images from the S2 and L8/9; while commercial high-resolution optical images, such as QuickBird and WorldView, were not included.

(2) The method used to remove incoherent noise in this study is based on SNR of cross-correlation and simple image processing techniques. Incoherent noise that cannot be fully removed based on SNR thresholds exhibits irregular values and locations. It would be necessary to develop an adaptive method to more effectively remove this kind of error. Moreover, iterative least square method can also identify gross error, which holds the potential to preserve more valid offset-tracking observations than the current method of removing gross errors in the pre-processing step.

(3) This study only selected three typical glacier sites in the North and South Poles, and HMA, where were dominated by glaciers or with the largest glaciers in the specific regions. It should be reminded that results of glacier velocity precision are not representative of the entire North and South Poles and/or HMA, but are only limited within the experimental regions, especially for regions with other types of land covers or glacier regions at other glacier zones instead of bare ice dominated area.

6 Conclusions

This study evaluates the precision of deriving glacier velocity from offset-tracking using S2 and L8/9 images. First gross errors (outliers) and systematic errors are evaluated and removed. Then the precision of offset-tracking at glacier and off-glacier regions are evaluated separately. For the glacier region, the flow rate time series is solved with a least square method based on the connected components, and the precision of its derived velocity time series was evaluated with the error propagation theory. The main conclusions are as follows. The offset-tracking in estimating glacier flow rates for both S2 and L8/9 platforms shows good precision, with S2

performing slightly better than L8/9. The RMSE of single-pair displacements for both platforms in the stable regions is mainly concentrated in the range of 0.4–1.2 m. Error propagation theory suggested that the RMSE of single-pair displacements at three selected glacier sites are 0.4–1.7 m for S2 and 1.7–2.9 m for L8/9, which are slightly higher than that of stable regions, due to the texture differences. Considering the redundant offset-tracking and different temporal intervals, the RMSEs of daily velocity are 0.06–0.21 $m \cdot d^{-1}$ for S2 and 0.16–0.29 $m \cdot d^{-1}$ for L8/9, the former is ~26% better than the latter. Therefore, S2 provides higher temporal resolution and higher precision in estimating glacier flow rate time series than L8/9.

Acknowledgement Sentinel-2 images are provided by ESA, Landsat-8/9 images and SRTM1 DEM are provided by NASA. GIMP velocity products, DEM products, Antarctic velocity and DEM products, and RGI 6.0 product are provided by NSIDC. We also thank the British Antarctic Survey (BAS) for providing Antarctic rock outcrop product. This research is supported by the National Natural Science Foundation of China (Grant no. 42371136), the Guangdong Basic and Applied Basic Research Foundation (Grant no. 2021B1515020032), and the Innovation Group Project of Southern Marine Science and Engineering Guangdong Laboratory (Zhuhai) (Grant no. 311022003). We also thank reviewer Dr. Xianwei Wang, one anonymous reviewer and Guest Editor Dr. Liming Jiang for their valuable comments on the manuscript.

Note This paper is a solicited manuscript of Special Issue "Observations and Simulations of Greenland Ice Sheet Melting" published on Vol.34, No.3 in September of 2023.

References

Ali E, Xu W, Ding X. 2020. Improved optical image matching time series inversion approach for monitoring dune migration in North Sinai Sand Sea: algorithm procedure, application, and validation. ISPRS J Photogramm Remote Sens, 164: 106-124, doi:10.1016/j.isprsjprs.2020.04.004.

Arendt A, Bliss A, Bolch T, et al. 2017. Randolph Glacier inventory–a dataset of global glacier outlines: Version 6.0: Technical report, global land ice measurements from space, doi:10.7265/4m1f-gd79.

Ayoub F, Leprince S, Avouac J P, et al. 2015. COSI-Corr: A software to monitor ground surface deformation from satellite imagery. Fourth Annual International Planetary Dunes Workshop, 1843: 8008.

Berthier E, Vadon H, Baratoux D, et al. 2005. Surface motion of mountain glaciers derived from satellite optical imagery. Remote Sens Environ, 95(1): 14-28, doi:10.1016/j.rse.2004.11.005.

Bindschadler R A, Scambos T A. 1991. Satellite-image-derived velocity field of an Antarctic ice stream. Science, 252(5003): 242-246, doi:10.1126/science.252.5003.242.

Debella-Gilo M, Kääb A. 2011. Sub-pixel precision image matching for measuring surface displacements on mass movements using normalized cross-correlation. Remote Sens Environ, 115(1): 130-142, doi:10.1016/j.rse.2010.08.012.

Debella-Gilo M, Kääb A. 2012. Locally adaptive template sizes for matching repeat images of Earth surface mass movements. ISPRS J Photogramm Remote Sens, 69: 10-28, doi:10.1016/j.isprsjprs.2012.02.002.

Delacourt C, Allemand P, Casson B, et al. 2004. Velocity field of the "La Clapière" landslide measured by the correlation of aerial and QuickBird satellite images. Geophys Res Lett, 31(15): L15619, doi:10.1029/2004gl020193.

Ding C, Feng G C, Li Z W, et al. 2016. Spatio-temporal error sources analysis and accuracy improvement in Landsat 8 image ground displacement measurements. Remote Sens, 8(11): 937, doi: 10.3390/rs8110937.

Ding C, Zhang L, Liao M S, et al. 2020. Quantifying the spatio-temporal patterns of dune migration near Minqin Oasis in northwestern China with time series of Landsat-8 and Sentinel-2 observations. Remote Sens Environment, 236: 111498, doi: 10.1016/j.rse.2019.111498.

Drusch M, Del Bello U, Carlier S, et al. 2012. Sentinel-2: ESA's optical high-resolution mission for GMES operational services. Remote Sens Environ, 120: 25-36, doi:10.1016/j.rse.2011.11.026.

Fahnestock M, Scambos T, Moon T, et al. 2016. Rapid large-area mapping of ice flow using Landsat 8. Remote Sens Environ, 185: 84-94, doi:10.1016/j.rse.2015.11.023.

Frey H, Machguth H, Huss M, et al. 2014. Estimating the volume of glaciers in the Himalayan-Karakoram region using different methods. Cryosphere, 8(6): 2313-2333, doi:10.5194/tc-8-2313-2014.

Gardner A S, Fahnestock M A, Scambos T A. MEaSUREs ITS_LIVE Landsat Image-Pair Glacier and Ice Sheet Surface Velocities: Version 1. Data archived at National Snow and Ice Data Center. 2019. doi: 10.5067/IMR9D3PEI28U

Gibson M J, Glasser N F, Quincey D J, et al. 2017. Changes in glacier surface cover on Baltoro glacier, Karakoram, north Pakistan, 2001–2012. J Maps, 13(2): 100-108, doi:10.1080/17445647.2016.1264319.

He L J, Feng G C, Feng Z X, et al. 2019. Coseismic displacements of 2016 MW7.8 Kaikoura, New Zealand earthquake, using Sentinel-2 optical images. Acta Geodaetica et Cartographica Sinica, 48(3): 339-351, doi: 10.11947/j.AGCS.2019.20170671 (in Chinese with English abstract).

Herman F, Anderson B, Leprince S. 2011. Mountain glacier velocity variation during a retreat/advance cycle quantified using sub-pixel analysis of ASTER images. J Glaciol, 57(202): 197-207, doi:10.3189/002214311796405942.

Hogg A E, Shepherd A, Gourmelen N, et al. 2016. Grounding line migration from 1992 to 2011 on Petermann glacier, North-West Greenland. J Glaciol, 62: 1104-1114, doi: 10.1017/jog.2016.83.

Jawak S D, Kumar S, Luis A J, et al. 2018. Evaluation of geospatial tools for generating accurate glacier velocity maps from optical remote sensing data. Proceedings, 2(7): 341, doi: 10.3390/ecrs-2-05154.

Kääb A, Winsvold S, Altena B, et al. 2016. Glacier remote sensing using Sentinel-2. part I: radiometric and geometric performance, and application to ice velocity. Remote Sens, 8(7): 598, doi:10.3390/rs8070598.

Konca A O, Leprince S, Avouac J P, et al. 2010. Rupture process of the 1999 mW 7.1 duzce earthquake from joint analysis of SPOT, GPS, InSAR, strong-motion, and teleseismic data: a supershear rupture with variable rupture velocity. Bull Seismol Soc Am, 100(1): 267-288, doi:10.1785/0120090072.

Leprince S, Barbot S, Ayoub F, et al. 2007. Automatic and precise orthorectification, coregistration, and subpixel correlation of satellite

images, application to ground deformation measurements. IEEE Trans Geosci Remote Sens, 45(6): 1529-1558, doi:10.1109/TGRS.2006.888937.

Leprince S, Berthier E, Ayoub F, et al. 2008a. Monitoring earth surface dynamics with optical imagery. EoS Transactions, 89(1): 1-2, doi:10.1029/2008eo010001.

Leprince S, Muse P, Avouac J P. 2008b. In-flight CCD distortion calibration for pushbroom satellites based on subpixel correlation. IEEE Trans Geosci Remote Sens, 46(9): 2675-2683, doi:10.1109/TGRS.2008.918649.

Li G, Mao Y, Feng X, et al. 2023. Monitoring ice flow velocity of Petermann glacier combined with Sentinel-1 and -2 imagery. Int J Appl Earth Obs Geoinformation, 121: 103374, doi:10.1016/j.jag.2023.103374.

Li J, Li Z, Wang C, et al. 2013. Estimation of the movement of Innerichik Glacier in south Tianshan Mountains using SAR offset tracking technique. Chin J Geophys, 56(4):1226-1236 (in Chinese with English abstract).

Li M, Zhang L, Dong J, et al. 2019. Characterization of pre- and post-failure displacements of the Huangnibazi landslide in Li County with multi-source satellite observations. Eng Geol, 257: 105140, doi:10.1016/j.enggeo.2019.05.017.

Li T, Chen Z, Li H, et al. 2020. Application of a new generation ice flow model, Ua, to the Amery Ice Shelf in Antarctica. J Glaciol Geocry, 42(1): 254-264.

Lin H, Li G, Cuo L, et al. 2017. A decreasing glacier mass balance gradient from the edge of the Upper Tarim Basin to the Karakoram during 2000–2014. Sci Rep, 7: 6712, doi:10.1038/s41598-017-07133-8.

Mayer C, Lambrecht A, Belò M, et al. 2006. Glaciological characteristics of the ablation zone of Baltoro glacier, Karakoram, Pakistan. Ann Glaciol, 43: 123-131, doi:10.3189/172756406781812087.

Michel R, Avouac J P. 2006. Coseismic surface deformation from air photos: the Kickapoo step over in the 1992 Landers rupture. J Geophys Res, 111(B3): B03408, doi:10.1029/2005jb003776.

Millan R, Mouginot J, Rabatel A, et al. 2022. Ice velocity and thickness of the world's glaciers. Nat Geosci, 15(2): 124-129, doi:10.1038/s41561-021-00885-z.

Mouginot J, Rignot E, Scheuchl B. 2014. Sustained increase in ice discharge from the Amundsen Sea Embayment, West Antarctica, from 1973 to 2013. Geophys Res Lett, 41(5): 1576-1584, doi:10.1002/2013gl059069.

Mouginot J, Rignot E, Scheuchl B, et al. 2017. Comprehensive annual ice sheet velocity mapping using Landsat-8, Sentinel-1, and RADARSAT-2 data. Remote Sens, 9(4): 364, doi:10.3390/rs9040364.

Paul F, Winsvold S, Kääb A, et al. 2016. Glacier remote sensing using Sentinel-2. part II: mapping glacier extents and surface facies, and comparison to Landsat 8. Remote Sens, 8(7): 575, doi:10.3390/rs8070575.

Peternel T, Kumelj Š, Oštir K, et al. 2017. Monitoring the Potoška planina landslide (NW Slovenia) using UAV photogrammetry and tachymetric measurements. Landslides, 14(1): 395-406, doi:10.1007/s10346-016-0759-6.

Rignot E, Steffen K. 2008. Channelized bottom melting and stability of floating ice shelves. Geophys Res Lett, 35(2): L02503, doi:10.1029/2007gl031765.

Rückamp M, Neckel N, Berger S, et al. 2019. Calving induced speedup of Petermann Glacier. J Geophys Res: Earth Surface, 124(1): 216-228, doi:10.1029/2018jf004775

Scherler D, Leprince S, Strecker M. 2008. Glacier-surface velocities in alpine terrain from optical satellite imagery—accuracy improvement and quality assessment. Remote Sens Environ, 112(10): 3806-3819, doi:10.1016/j.rse.2008.05.018.

Song H. 2021. Monitoring and application of regional landslide deformation based on optical and SAR image offset estimation. Master's thesis, Guangzhou: Guangzhou University (in Chinese with English abstract).

Spergel J J, Kingslake J, Creyts T, et al. 2021. Surface meltwater drainage and ponding on Amery Ice Shelf, East Antarctica, 1973–2019. J Glaciol, 67(266): 985-998, doi:10.1017/jog.2021.46.

Van Puymbroeck N, Michel R, Binet R, et al. 2000. Measuring earthquakes from optical satellite images. Appl Opt, 39(20): 3486-3494, doi:10.1364/AO.39.003486.

Young N. 1989. Surface velocities of Denman Glacier, Antarctica, derived from Landsat imagery. A Glaciol, 12: 218, doi:10.1017/s0260305500007497.

Zheng Q. 2015. Extraction of ground horizontal displacement and its time series information based on optical image data. Master's thesis, Beijing: Geological Research Institute, China Earthquake Administration (in Chinese with English abstract).

Zitová B, Flusser J. 2003. Image registration methods: a survey. Image Vis Comput, 21(11): 977-1000, doi:10.1016/s0262-8856(03)00137-9.